

Deep crustal contact between the Pamir and Tarim Basin deduced from receiver functions

Qiang Xu¹, Junmeng Zhao², Xiaohui Yuan³, Hongbing Liu², Changhui Ju², Bernd Schurr⁴, and Wasja Bloch⁴

¹Institute of Tibetan Plateau Research

²Institute of Tibetan Plateau Research, Chinese Academy of Sciences

³schurr@gfz-potsdam.de

⁴Deutsches GeoForschungsZentrum GFZ

November 22, 2022

Abstract

The deep crustal deformation in the east Pamir in response to Cenozoic collision with the Tien Shan and Tarim Basin is so far poorly constrained. We present new insights into the crustal structure of the east Pamir and the surrounding regions using P receiver functions from 40 temporary and permanent seismic stations. The crustal thickness reaches a maximum of 88 km beneath the central and southern east Pamir and decreases sharply to 50-60 km along the southern Tien Shan and to 41-50 km below Tarim Basin. The most prominent crustal structures involve a double Moho and two Moho offsets, which suggest that the crustal deformation in the east Pamir is controlled by multiple mechanisms, including delamination of Asian lower crust below the central east Pamir, pure shear shortening along the northeastern margin between the Pamir and Tarim/Tien Shan and eastward underthrusting of Pamir lower crust beneath the southern east Pamir.

Hosted file

essoar.10506378.1.doc available at <https://authorea.com/users/538046/articles/599500-deep-crustal-contact-between-the-pamir-and-tarim-basin-deduced-from-receiver-functions>

1 Deep crustal contact between the Pamir and Tarim Basin deduced from
2 receiver functions

3 Qiang Xu^{1,2}, Junmeng Zhao^{1,2}, Xiaohui Yuan³, Hongbing Liu¹, Changhui Ju¹, Bernd
4 Schurr³, Wasja Bloch³

5 ¹ Key Laboratory of Continental Collision and Plateau Uplift, Institute of Tibetan
6 Plateau Research, Chinese Academy of Sciences, Beijing 100101, China

7 ² CAS Center for Excellence in Tibetan Plateau Earth Sciences, Beijing 100101, China

8 ³ Deutsches GeoForschungsZentrum GFZ, Telegrafenberg, Potsdam 14473, Germany

9 *Corresponding authors: zhaojm@itpcas.ac.cn; xuqiang@itpcas.ac.cn

10

11 **Key Points**

- 12 · The Asian lower crust is delaminated beneath the central east Pamir
13 · The northeast Pamir crust extends into the Tarim Basin and thickens by pure shear
14 shortening
15 · The southeast Pamir crust is underthrusting beneath West Kunlun Shan and Tarim
16 Basin

17

18 **Abstract**

19 The deep crustal deformation in the east Pamir in response to Cenozoic collision with
20 the Tien Shan and Tarim Basin is so far poorly constrained. We present new insights
21 into the crustal structure of the east Pamir and the surrounding regions using P
22 receiver functions from 40 temporary and permanent seismic stations. The crustal

23 thickness reaches a maximum of 88 km beneath the central and southern east Pamir
24 and decreases sharply to 50-60 km along the southern Tien Shan and to 41-50 km
25 below Tarim Basin. The most prominent crustal structures involve a double Moho and
26 two Moho offsets, which suggest that the crustal deformation in the east Pamir is
27 controlled by multiple mechanisms, including delamination of Asian lower crust
28 below the central east Pamir, pure shear shortening along the northeastern margin
29 between the Pamir and Tarim/Tien Shan and eastward underthrusting of Pamir lower
30 crust beneath the southern east Pamir.

31

32 Plain Language Summary

33 The Pamir orogen is located at the leading edge of the Indo-Asian collision zone and
34 has translated northward by about 300 km with respect to the Himalaya-Tibetan
35 plateau since the Late Cenozoic. It protruded the formerly connected Tajik and Tarim
36 basins and formed a curvilinear front with Tajik Basin to the west, Tien Shan to the
37 north and Tarim Basin to the east. Previous studies revealed that the Pamir is
38 underthrust by the Asian crust from the west and from the north; however, it is still
39 unclear how the contact between Pamir and the Tarim basin crust looks like. This
40 study elucidates the deep crustal interaction between the two tectonic blocks by
41 receiver functions with data from a recent seismic experiment in the region. The
42 Pamir crust is extended into the western tip of the Tarim basin and is thickened by
43 pure shear, while in the south it is subducted beneath the West Kunlun Shan and Tarim
44 Basin into the mantle to a depth of >100 km.

45

46 **Keywords:** east Pamir, Tarim Basin, receiver functions, crustal structure, continental
47 crust subduction, delamination

48

49 1. Introduction

50 The Pamir orogen lies north of the western Himalayan syntaxis in the India-Asia
51 collision zone (Figure 1) and attains an elevation of ≥ 4 km and a crustal thickness of
52 65-75 km by absorbing ~55-64% Cenozoic shortening within a relatively narrow
53 north-south distance compared to the main Tibetan Plateau (Schmidt et al., 2011). A
54 major orocline has formed due to the northward displacement of the Pamir by at least
55 300 km relative to Tibet and the Hindu Kush, with bending of this orogen associated
56 with several well-developed thrusting and strike-slip faults along its margins (Figure
57 1); these include the sinistral Darvaz-Karakul strike-slip fault bounding Tajik Basin to
58 the west, the dextral Kashgar-Yecheng Transfer System (KYTS) bounding Tarim
59 Basin to the east and the Main Pamir Thrust (MPT) bounding Alai Valley to the north
60 (Figure 1). Structurally, the Pamir comprises a series of terranes that were accreted
61 during the Paleozoic and Early Mesozoic. The Pamir can be divided into the North,
62 Central and South Pamir, which are separated by the Tanymas and Rushan-Pshart
63 sutures (Schwab et al., 2004).

64

65 Intense intermediate-depth seismicity has been observed beneath the Pamir and Hindu
66 Kush (Sippl et al., 2013a), which is interpreted as evidence for ongoing

67 intracontinental subduction (Schneider et al., 2013; Sobel et al., 2013) or forced
68 delamination(Kufner et al., 2016). The opposite dips of deep earthquakes beneath the
69 Pamir and Hindu Kush have invoked different interpretations about the plate
70 configuration ranging from a single contorted slab of Indian (Pavlis & Das, 2000), or
71 Asian origin (Perry et al., 2019) to a two-slab model that involves the eastward to
72 southward subduction/delamination of Asian lithosphere in a tight 90° arc beneath the
73 Pamir and northward subduction of Indian lithosphere beneath the Hindu Kush
74 (Kufner, et al., 2016; Negredo et al., 2007). A receiver function image along a
75 north-south profile at ~73.8° E reveals that these intermediate-depth earthquakes
76 occur in a 10 -15 km thick low velocity zone (LVZ) possibly associated with the
77 southward subduction of Asian lower crust reaching a depth of 150 km (Schneider, et
78 al., 2013), consistent with the results of local earthquake tomography and guided
79 waves analyses (Mechie et al., 2019; Sippl et al., 2013b). Recently, an additional
80 NW-SE trending intermediate-depth earthquake zone has been identified south of the
81 eastern termination of E-W striking segment of the Pamir seismic zone, roughly
82 parallel to the Karakax fault (KXF) (Bloch et al., 2020), which suggests a different
83 and still ambiguous origin compared to the Pamir-Hindu Kush seismic zone.

84

85 A previous receiver function analysis shows a double Moho structure at 50-90 km
86 depth, which hints at underthrusting of the Tajik lower crust beneath western Pamir
87 (Schneider et al., 2019). Plate motion vectors and seismotectonic analysis testify that
88 crustal materials flow outward from the interior of the Pamir towards the western

89 flanks and/or extrude upward along a series of thrust faults (Schurr et al., 2014).
90 Conversely, the rigid Tarim crust may hinder eastward extrusion of the east Pamir
91 (Metzger et al., 2020; Schurr, et al., 2014). The dextral KYTS as the boundary
92 between the east Pamir and Tarim Basin is supposed to be the eastern edge of
93 subducting Asian lithosphere (Sobel, et al., 2013). These studies provide no evidence
94 for subduction of Tarim Basin beneath the east Pamir, but how the crust deforms in
95 the east Pamir facing the obstruction of the Tarim Basin remains insufficiently
96 constrained, partly due to limited data available in this region.

97

98 In this study, we use P receiver functions (PRFs) derived from a recently deployed
99 temporary seismic array and permanent stations to investigate the crustal structure
100 beneath the east Pamir and the adjacent region at a higher resolution than has
101 previously been possible. Our crustal thickness and V_p/V_s ratio observations provide
102 new insights into the crustal deformation patterns in the east Pamir under the
103 resistance of Tarim Basin and Tien Shan during intracontinental orogenesis.

104

105 2. Data and methods

106 The three-component seismograms used in this study were recorded at 40 broadband
107 stations during the period from 2015 to 2017, consisting of 31 stations in a temporary
108 two-dimensional (2-D) seismic array of the east Pamir seismic experiment (FDSN
109 code 8H; (Yuan et al., 2018)) and 9 permanent stations from China Earthquake
110 Administration (CEA) network (Zheng et al., 2010) (Figure 1). We selected

111 teleseismic earthquakes with signal-to-noise ratios on the vertical component ≥ 2.5 ,
112 body-wave magnitudes (M_b) ≥ 5.5 , and epicentral distances in the $30\text{-}95^\circ$ range for the
113 PRF computations.

114

115 PRF analysis is one of the most frequently used techniques to explore the seismic
116 structures underneath a seismic station using the P-to-S (Ps) conversions and
117 associated multiples that originate from discontinuities at different depths. The raw
118 Z-N-E traces of each event are rotated into the ray-based P-SV-SH coordinate system
119 using the theoretical back azimuth and incident angle. The P component is then
120 deconvolved from the SV component using a time domain Wiener filtering method to
121 produce the SV receiver function (PRF) (Yuan et al., 1997). A visual quality control
122 was carried out on all of the PRFs to eliminate outliers with significant oscillations or
123 strong amplitudes. Finally, a total of 3153 PRFs, obtained from 270 teleseismic events,
124 were retained for subsequent processing.

125

126 We estimate the crustal thickness (H) and V_p/V_s ratio (κ) at each station using the
127 delay times of the Moho Ps and PpPs phases (Xu et al., 2017). This algorithm avoids
128 the effects of multiple extremes on the energy surface that are often confronted by the
129 popular H - κ stacking method in complex orogenic areas (Murodov et al., 2018; Zhu &
130 Kanamori, 2000), thereby yielding more robust solutions for H and κ . We manually
131 pick both delay times on two individual sum traces that are produced by stacking all
132 of the PRFs from each station after a moveout correction for the Ps and PpPs phases,

133 respectively. To identify the PpPs phase reliably, we pick this phase within a predicted
134 time window based on the picked delay time of the Moho Ps conversion and two κ
135 values of 1.6 and 2.0. The two standard deviations obtained using the bootstrap
136 resampling technique (Xu, et al., 2017), are considered as the uncertainties for both H
137 and κ (Table S1).

138

139 To delineate the morphology of the subsurface discontinuities, three cross sections are
140 constructed using a common conversion point (CCP) stacking technique (Yuan et al.,
141 2000). The amplitudes of each PRF are back projected along their ray paths to their
142 respective depths within a Fresnel zone around the piercing points. We perform the
143 ray tracing and time-depth conversion using a 2-D velocity model along each cross
144 section which is interpolated from the 1-D modified IASP91 model for each station,
145 whereby the crustal structure has been changed using the P wave velocity model from
146 a wide-angle reflection/refraction profile within the study area and the resulting
147 V_p/V_s ratio (Zhang et al., 2002). Especially, the revised 1-D model includes a 5 km
148 thick sedimentary layer with $V_p = 3.20$ km/s and $V_s = 1.82$ km/s for the stations at
149 <1.5 km elevation in Tarim Basin,

150

151 3. Results

152 Figure 2 exhibits PRF stacks for 38 stations, together with the carefully picked delay
153 times of the Moho Ps and PpPs phases. The Moho Ps and PpPs conversions arrive at
154 5.3 to 11.5 s and 18.2 to 38.1 s, respectively. Stations KSH and EP16 (Figure S1) are

155 not included due to ambiguous Moho Ps signals caused by strong sedimentary
156 reverberations. We simultaneously obtain H and κ values for 35 stations, for which
157 both the Moho Ps and PpPs are clearly visible. For three other stations, we could not
158 determine the κ values because the Moho PpPs phases are unclear. We only estimate
159 the H values using the arrival times of the Moho Ps conversions and κ values from
160 their adjacent stations (Table S1).

161

162 We generate a regional-scale crustal thickness map across the Pamir and the
163 surrounding region by combining previously published results with the measurements
164 obtained in this study (Table S2 and Figure 3a). Details of crustal thickness variations
165 outside our study region can be found in Schneider et al. (2019) and Zhang et al.
166 (2020). The map reveals two deep Moho regions (called Moho troughs), one in the
167 western central Pamir along the boundary region of the Pamir with the Tajik basin
168 (Schneider et al., 2019), the other in the east Pamir along the West Kunlun Shan, the
169 boundary region with the Tarim basin. Both Moho troughs are parallel to
170 intermediate-depth seismic zones. In this paper we focus on our observations in the
171 east Pamir. The resulting H values decrease from 67-88 km beneath the east Pamir to
172 50-60 km along the southern Tien Shan and 41-50 km beneath the Tarim Basin. The
173 thickest crust (up to 88 km) is observed in the southeastern Pamir along the West
174 Kunlun Shan and an elongated region of thicker crust with a thickness ranging from
175 68 to 74 km in the northeastern margin of the Pamir extends northeastward to the
176 Pamir Frontal Thrust (PFT). Figure 3b indicates that the κ values vary significantly,

177 ranging from 1.68 to 1.89 with an average uncertainty of 0.02. The low to moderate κ
178 values of 1.68-1.81 are mainly distributed throughout the east Pamir, suggesting felsic
179 and intermediate bulk crustal compositions possibly resulted from delamination or
180 foundering of the mafic lower crust. The high κ values of more than 1.81 in Tarim
181 Basin are likely caused by the thick sedimentary sequences, whereas those in the east
182 Pamir and southern Tien Shan may be the result of fractured damage zones and/or
183 partial melt within the crust.

184

185 Strong positive conversions at depths of 40-90 km, which are interpreted to be
186 indicative of the Moho, are clearly identified in the CCP stacking images along three
187 selected cross sections (Figure 4). Superimposing the crustal thicknesses over the
188 three CCP images reveals a good agreement with the lateral variations in Moho depth,
189 giving confidence that the imaged Moho structure is credible. A Moho offset of at
190 least 12 km appears below the surface trace of the PFT along profile A-A', separating
191 a sub-horizontal Moho at depths of 70-78 km in the south from a shallowly
192 south-dipping Moho at 50-58 km depth in the north. A double Moho structure is
193 observed below the surface trace of the KXF along profile B-B'; the deeper Moho
194 reaches a depth of 88 km and continues to dip eastward, while the shallower Moho at
195 depths of 62-66 km gradually shallows to 45 km beneath Tarim Basin. The individual
196 PRFs at stations EP27 and EP30 (Figure S1) which are located above this double
197 structure are shown in Figure S2. Profile C-C' is characterized by another significant
198 Moho offset of about 18 km below Muztagh Ata (MA); this offset separates a

199 south-dipping Moho at 60-88 km depth in the north from a sub-horizontal Moho at
200 70-78 km depth in the south.

201

202 We generate the maps of the hit counts at each bin of the CCP stacks along three cross
203 sections (Figure S3). The hit count represents the PRF ray coverage beneath each
204 profile. The ray coverage of our imaged Moho structure is quite good with hit counts
205 more than 100, which suggests that the distinguishing features of Moho described
206 above is reliable.

207

208 4. Discussion

209 The most striking features observed in our CCP stacking images are the presence of a
210 double Moho structure and two Moho offsets, which contribute fresh insights into the
211 dynamic processes of crustal deformation in the east Pamir and the surrounding
212 region. Figure 5 summarizes our structural interpretation of the imaged crustal
213 structure.

214

215 The Moho offset observed below the PFT in northeastern (NE) Pamir marks the
216 tectonic boundary between the Pamir and the Tarim Basin. Under the regional tectonic
217 settings of the northward indentation of the Pamir and the resistance of the strong
218 Tarim lithosphere, the development of the Moho offset suggests that pure shear
219 shortening is responsible for the crustal thickening in the NE Pamir. This
220 interpretation is consistent with stratigraphic and magnetostratigraphic data,

221 suggesting that the PFT became the leading edge of the Pamir deformation around 5-6
222 Ma and accommodated the Quaternary shortening along the NE margin of the Pamir
223 (Thompson et al., 2015). Analogous scenarios have also been reported in the
224 transitional regions between the South-Central Tien Shan and northern Tarim Basin
225 (Zhang et al., 2020), and along the boundary between western Tibet and the southern
226 Tarim Basin (Murodov, et al., 2018). Furthermore, a similar Moho offset is
227 inconspicuous in the North Pamir-Tien shan collision zone, which is west of the
228 elongated region of thicker crust. The reasons for this phenomenon could be that the
229 lithospheric strength of Tien shan is weaker than that beneath Tarim Basin
230 (Bagdassarov et al., 2011), and much of the shortening between North Pamir and the
231 southern Tien Shan has migrated into the Tien Shan east of 75°E since 10 Ma (Sobel
232 et al., 2006).

233

234 Previous studies have demonstrated the delamination of Asian lower crust beneath
235 North and Central Pamir west of our study area (Schneider et al., 2013; Kufner, et al.,
236 2016). Following these studies and considering the dominant E-W distribution of
237 intermediate-depth seismicity, we suggest that the Moho offset observed beneath MA
238 represents the eastward expansion of the delaminated Asian lower crust terminating at
239 the KYTS. This scenario of no overlapping Moho and sinking Asian lower crust is in
240 more accordance with delamination than classical subduction (Bird, 1979), because
241 the downgoing Asian crust is primarily driven by the indentation of Indian lithosphere
242 and negative buoyancy due to the eclogitization of Asian lower crust (Schneider et al.,

243 2013; Kufner, et al., 2016). Alternatively, large-scale asthenospheric flow, which has
244 been inferred from shear wave splitting measurements, may have also delivered
245 relatively hot materials into the crust through a crustal tear between Tarim Basin and
246 the Asian lithosphere, possibly facilitating the delamination of Asian lower crust (Bird,
247 1979; Kufner et al., 2018). Decompression- and dehydration-related melts that form
248 following the delamination of eclogitized crust and mantle lithosphere can intrude
249 upward into the middle and lower crust. These intrusions can cause crustal anatexis,
250 which is thought to have contributed to rapid exhumation of the Muztagh Ata and
251 Kongur Shan domes, which are possibly associated with successive stages of
252 delamination of the Asian lithosphere (Li et al., 2020; Thiede et al., 2013).

253

254 The most intriguing structure of our observations is a double Moho in the southern
255 portion of the east Pamir. In conjunction with the NW-SE trending intermediate-depth
256 seismicity, we suggest that this double Moho structure provides direct evidence for
257 eastward underthrusting of the Pamir lower crust beneath the West Kunlun Shan and
258 Tarim Basin. Conversely, a similar structure identified below western Pamir has been
259 interpreted to represent underthrusting of the Tajik lower crust (Schneider, et al.,
260 2019). The spatial relationship of the two Moho troughs with the intermediate-depth
261 seismic zones implies that underthrusting involves crust. In the west Pamir, the Moho
262 trough is located northwest of the seismic zone, suggesting a southeastward
263 underthrusting of the Asian crust (Schneider, et al., 2019). In the east Pamir, the Moho
264 trough is to the west of the seismic zone, indicating an eastward underthrusting of the

265 Pamir crust. Our interpretation is compatible with sedimentary and
266 magnetostratigraphic analyses along the Aertashi section, which indicate
267 eastward-directed thrusting of the Pamir onto Tarim Basin and an rotation from
268 approximately N-S to E-W in the maximum strain orientation at 15 Ma (Blayney et al.,
269 2019). Crustal xenoliths from the Dunkeldik volcanic field erupted at ~11 Ma in the
270 southeastern Pamir suggest that Gondwanan Pamir crust was subducted to depths of
271 90-100 km beneath Eurasia (Hacker et al., 2005), which is analogous to our
272 interpretation. A notable high-velocity anomaly imaged below 180 km depth has been
273 interpreted as northward underthrusting Indian mantle lithosphere (Li et al., 2008),
274 which may provide the driving force for the development of the underthrusting
275 structure described here.

276

277 5. Conclusions

278 We obtain the crustal structure below the east Pamir and the adjacent region by
279 applying PRF techniques to teleseismic waveforms recorded at a temporary 2-D
280 seismic array and the permanent stations. The crustal thickness ranges from 67-88 km
281 beneath the east Pamir and reduces to 50-60 km along the southern Tien Shan and
282 41-50 km in the Tarim basin. Our depth migration images indicate the presence of a
283 double Moho structure and two Moho offsets, which shed new light on crustal
284 deformation patterns in the east Pamir. We suggest that pure shear shortening accounts
285 for crustal thickening in NE Pamir, while delamination of Asian lower crust and
286 eastward underthrusting of Pamir lower crust dominate the deformation processes in

287 the central and southern portions of the east Pamir, respectively.

288

289 Acknowledgments

290 This research was funded by the Strategic Priority Research Program of Chinese
291 Academy of Sciences (Grant No. XDA20070302) and the CaTeNA project of the
292 German Federal Ministry of Science and Education (support code 03G0878A). The
293 temporary seismic experiment (8H) was partly supported by the expedition fund from
294 Deutsches GeoForschungsZentrum GFZ. Temporary instruments were provided by
295 the Geophysical Instrument Pool Potsdam (GIPP). Seismic data are archived at the
296 GEOFON data center (Yuan, et al., 2018) and at the Institute of Tibetan Plateau
297 Research, Chinese Academy of Sciences. We thank the Data Management Centre of
298 the China National Seismic Network at the Institute of Geophysics, China Earthquake
299 Administration, for providing waveform data of permanent stations (SEISDMC,
300 doi:10.11998/SeisDmc/SN, <http://www.seisdmc.ac.cn/>; Zheng et al., 2010).

301

302 References

- 303 Bagdassarov, N., Batalev, V., & Egorova, V. (2011). State of lithosphere beneath Tien
304 Shan from petrology and electrical conductivity of xenoliths. *Journal of*
305 *Geophysical Research-Solid Earth*, *116*, B01202.
306 <https://doi.org/10.1029/2009jb007125>
- 307 Bird, P. (1979). Continental Delamination and the Colorado Plateau. *Journal of*
308 *Geophysical Research*, *84*(B13), 7561-7571.

309 <https://doi.org/10.1029/Jb084ib13p07561>

310 Blayney, T., Dupont-Nivet, G., Najman, Y., Proust, J. N., Meijer, N., Roperch, P.
311 (2019). Tectonic Evolution of the Pamir Recorded in the Western Tarim Basin
312 (China): Sedimentologic and Magnetostratigraphic Analyses of the Aertashi
313 Section. *Tectonics*, 38(2), 492-515. <https://doi.org/10.1029/2018TC005146>

314 Bloch, W., Schurr, B., Yuan, X., Ratschbacher, L., Abdulhameed, A., Kufner, S.-K.,
315 Xu, Q., Zhao, J. (2020). Structure of the deep lithosphere between Pamir and
316 Tarim, *Geology* (submitted).

317 Hacker, B., Luffi, P., Lutkov, V., Minaev, V., Ratschbacher, L., Plank, T. (2005).
318 Near-ultrahigh pressure processing of continental crust: Miocene crustal
319 xenoliths from the Pamir. *Journal of Petrology*, 46(8), 1661-1687.
320 <https://doi.org/10.1093/petrology/egi030>

321 Kufner, S. K., Eken, T., Tilmann, F., Schurr, B., Yuan, X. H., Mechie, J. (2018).
322 Seismic Anisotropy Beneath the Pamir and the Hindu Kush: Evidence for
323 Contributions From Crust, Mantle Lithosphere, and Asthenosphere. *Journal of*
324 *Geophysical Research-Solid Earth*, 123(12), 10727-10748.
325 <https://doi.org/10.1029/2018JB015926>

326 Kufner, S. K., Schurr, B., Sippl, C., Yuan, X. H., Ratschbacher, L., Akbar, A. S. M.
327 (2016). Deep India meets deep Asia: Lithospheric indentation, delamination
328 and break-off under Pamir and Hindu Kush (Central Asia). *Earth and*
329 *Planetary Science Letters*, 435, 171-184.
330 <https://doi.org/10.1016/j.epsl.2015.11.046>

- 331 Li, C., Van der Hilst, R. D., Meltzer, A. S., & Engdahl, E. R. (2008). Subduction of
332 the Indian lithosphere beneath the Tibetan Plateau and Burma. *Earth and*
333 *Planetary Science Letters*, 274(1-2), 157-168.
334 <https://doi.org/10.1016/j.epsl.2008.07.016>
- 335 Li, Y. P., Robinson, A. C., Lapen, T. J., Righter, M., & Stevens, M. K. (2020).
336 Muztaghata Dome Miocene Eclogite Facies Metamorphism: A Record of
337 Lower Crustal Evolution of the NE Pamir. *Tectonics*, 39, e2019TC005917.
338 <https://doi.org/10.1029/2019TC005917>
- 339 Mechie, J., Schurr, B., Yuan, X., Schneider, F., Sippl, C., Minaev, V. (2019).
340 Observations of guided waves from the Pamir seismic zone provide additional
341 evidence for the existence of subducted continental lower crust.
342 *Tectonophysics*, 762, 1-16. <https://doi.org/10.1016/j.tecto.2019.04.007>
- 343 Metzger, S., Ischuk, A., Deng, Z., Ratschbacher, L., Perry, M., Kufner, S. K. (2020).
344 Dense GNSS Profiles Across the Northwestern Tip of the India - Asia
345 Collision Zone: Triggered Slip and Westward Flow of the Peter the First
346 Range, Pamir, Into the Tajik Depression. *Tectonics*, 39(2), e2019TC005797.
347 <https://doi.org/10.1029/2019TC005797>
- 348 Murodov, D., Zhao, J. M., Xu, Q., Liu, H. B., & Pei, S. P. (2018). Complex N-S
349 variations in Moho depth and $V(p)/V(s)$ ratio beneath the western Tibetan
350 Plateau as revealed by receiver function analysis. *Geophysical Journal*
351 *International*, 214(2), 895-906. <https://doi.org/10.1093/gji/ggy170>
- 352 Negredo, A. M., Replumaz, A., Villasenor, A., & Guillot, S. (2007). Modeling the

353 evolution of continental subduction processes in the Pamir-Hindu Kush region.
354 *Earth and Planetary Science Letters*, 259(1-2), 212-225.
355 <https://doi.org/10.1016/j.epsl.2007.04.043>

356 Pavlis, G. L., & Das, S. (2000). The Pamir-Hindu Kush seismic zone as a strain
357 marker for flow in the upper mantle. *Tectonics*, 19(1), 103-115.
358 <https://doi.org/10.1029/1999tc900062>

359 Perry, M., Kakar, N., Ischuk, A., Metzger, S., Bendick, R., Molnar, P. (2019). Little
360 Geodetic Evidence for Localized Indian Subduction in the Pamir-Hindu Kush
361 of Central Asia. *Geophysical Research Letters*, 46(1), 109-118.
362 <https://doi.org/10.1029/2018GL080065>

363 Schmidt, J., Hacker, B. R., Ratschbacher, L., Stubner, K., Stearns, M., Kylander-Clark,
364 A. (2011). Cenozoic deep crust in the Pamir. *Earth and Planetary Science
365 Letters*, 312(3-4), 411-421. <https://doi.org/10.1016/j.epsl.2011.10.034>

366 Schneider, F. M., Yuan, X., Schurr, B., Mechie, J., Sippl, C., Haberland, C. (2013).
367 Seismic imaging of subducting continental lower crust beneath the Pamir.
368 *Earth and Planetary Science Letters*, 375, 101-112.
369 <https://doi.org/10.1016/j.epsl.2013.05.015>

370 Schneider, F. M., Yuan, X., Schurr, B., Mechie, J., Sippl, C., Kufner, S. K. (2019). The
371 Crust in the Pamir: Insights From Receiver Functions. *Journal of Geophysical
372 Research-Solid Earth*, 124(8), 9313-9331.
373 <https://doi.org/10.1029/2019JB017765>

374 Schurr, B., Ratschbacher, L., Sippl, C., Gloaguen, R., Yuan, X. H., & Mechie, J.

375 (2014). Seismotectonics of the Pamir. *Tectonics*, 33(8), 1501-1518.
376 <https://doi.org/10.1002/2014TC003576>

377 Schwab, M., Ratschbacher, L., Siebel, W., Williams, M. M., Minaev, V., Lutkov, V.
378 (2004). Assembly of the Pamirs: Age and origin of magmatic belts from the
379 southern Tien Shan to the southern Pamirs and their relation to Tibet. *Tectonics*,
380 23(4), TC4002. <https://doi.org/10.1029/2003TC001583>

381 Sippl, C., Schurr, B., Yuan, X., Mechie, J., Schneider, F. M., Gadoev, M. (2013a).
382 Geometry of the Pamir-Hindu Kush intermediate-depth earthquake zone from
383 local seismic data. *Journal of Geophysical Research-Solid Earth*, 118(4),
384 1438-1457. <https://doi.org/10.1002/jgrb.50128>

385 Sippl, C., Schurr, B., Tympel, J., Angiboust, S., Mechie, J., Yuan, X. (2013b). Deep
386 burial of Asian continental crust beneath the Pamir imaged with local
387 earthquake tomography. *Earth and Planetary Science Letters*, 384, 165-177.
388 <https://doi.org/10.1016/j.epsl.2013.10.013>

389 Sobel, E. R., Chen, J., & Heermance, R. V. (2006). Late Oligocene-Early Miocene
390 initiation of shortening in the Southwestern Chinese Tian Shan: Implications
391 for Neogene shortening rate variations. *Earth and Planetary Science Letters*,
392 247(1-2), 70-81. <https://doi.org/10.1016/j.epsl.2006.03.048>

393 Sobel, E. R., Chen, J., Schoenbohm, L. M., Thiede, R., Stockli, D. F., Sudo, M. (2013).
394 Oceanic-style subduction controls late Cenozoic deformation of the Northern
395 Pamir orogen. *Earth and Planetary Science Letters*, 363, 204-218.
396 <https://doi.org/10.1016/j.epsl.2012.12.009>

397 Thiede, R. C., Sobel, E. R., Chen, J., Schoenbohm, L. M., Stockli, D. F., Sudo, M.
398 (2013). Late Cenozoic extension and crustal doming in the India-Eurasia
399 collision zone: New thermochronologic constraints from the NE Chinese
400 Pamir. *Tectonics*, 32(3), 763-779. <https://doi.org/10.1002/tect.20050>

401 Thompson, J. A., Burbank, D. W., Li, T., Chen, J., & Bookhagen, B. (2015). Late
402 Miocene northward propagation of the northeast Pamir thrust system,
403 northwest China. *Tectonics*, 34(3), 510-534.
404 <https://doi.org/10.1002/2014TC003690>

405 Xu, Q., Zhao, J. M., Yuan, X. H., Liu, H. B., & Pei, S. P. (2017). Detailed
406 Configuration of the Underthrusting Indian Lithosphere Beneath Western Tibet
407 Revealed by Receiver Function Images. *Journal of Geophysical*
408 *Research-Solid Earth*, 122(10), 8257-8269.
409 <https://doi.org/10.1002/2017JB014490>

410 Yuan, X., Schurr, B., Bloch, W., Xu, Q., & Zhao, J. (2018). The 8H East Pamir
411 seismic network. *GFZ Data Services*. <https://doi.org/10.14470/3U7560589977>

412 Yuan, X., Sobolev, S. V., Kind, R., Oncken, O., Bock, G., Asch, G. (2000). Subduction
413 and collision processes in the Central Andes constrained by converted seismic
414 phases. *Nature*, 408(6815), 958-961

415 Yuan, X. H., Ni, J., Kind, R., Mechie, J., & Sandvol, E. (1997). Lithospheric and
416 upper mantle structure of southern Tibet from a seismological passive source
417 experiment. *Journal of Geophysical Research-Solid Earth*, 102(B12),
418 27491-27500. <https://doi.org/10.1029/97jb02379>

419 Zhang, B. F., Bao, X. W., & Xu, Y. X. (2020). Distinct Orogenic Processes in the
420 South- and North-Central Tien Shan From Receiver Functions. *Geophysical*
421 *Research Letters*, 47(6), e2019GL086941.
422 <https://doi.org/10.1029/2019GL086941>

423 Zhang, X. K., Zhao, J. R., Zhang, C. K., Ren, Q. F., Nie, W. Y., Cheng, S. X. (2002).
424 Crustal structure at the northeast side of the Pamirs. *Chinese Journal of*
425 *Geophysics-Chinese Edition*, 45(5), 665-671

426 Zheng, X. F., Yao, Z. X., Liang, J. H., & Zheng, J. (2010). The Role Played and
427 Opportunities Provided by IGP DMC of China National Seismic Network in
428 Wenchuan Earthquake Disaster Relief and Researches. *Bulletin of the*
429 *Seismological Society of America*, 100(5B), 2866-2872.
430 <https://doi.org/10.1785/0120090257>

431 Zhu, L., & Kanamori, H. (2000). Moho depth variation in southern California from
432 teleseismic receiver functions. *Journal of Geophysical Research: Solid Earth*,
433 105(B2), 2969-2980. <https://doi.org/10.1029/1999JB900322>

434

435

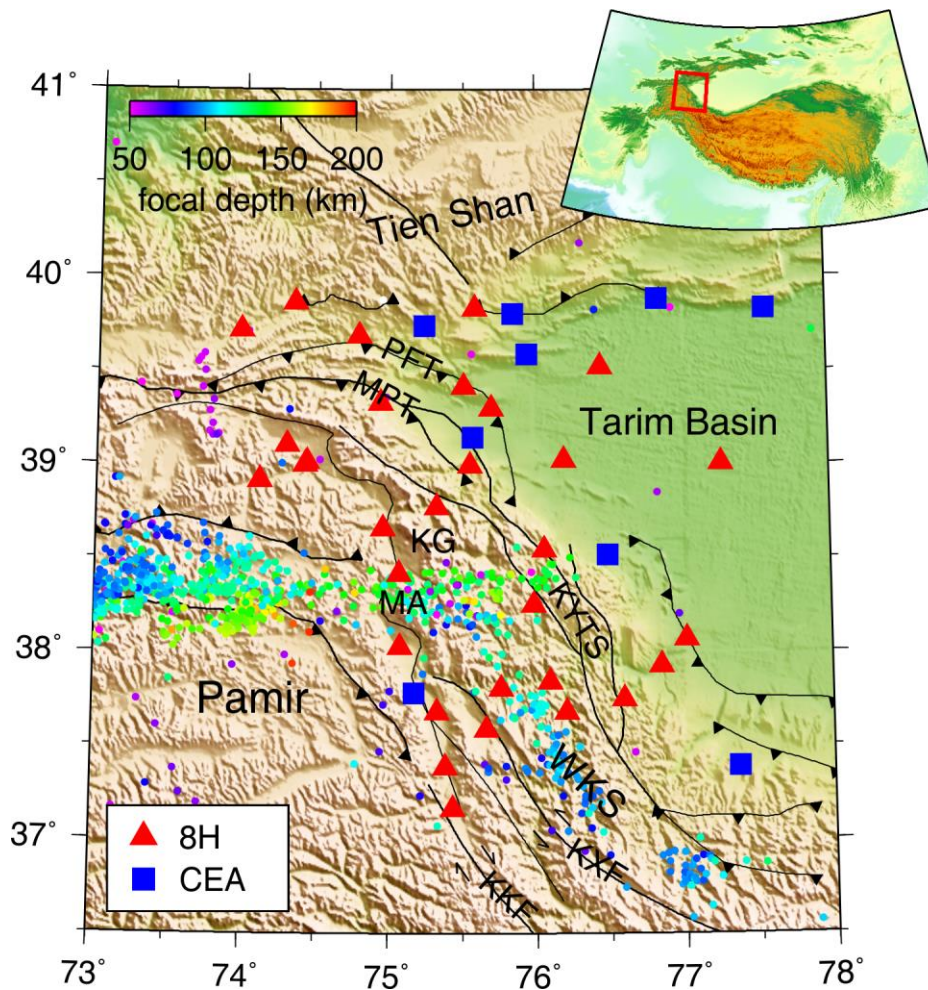
436

437

438

439

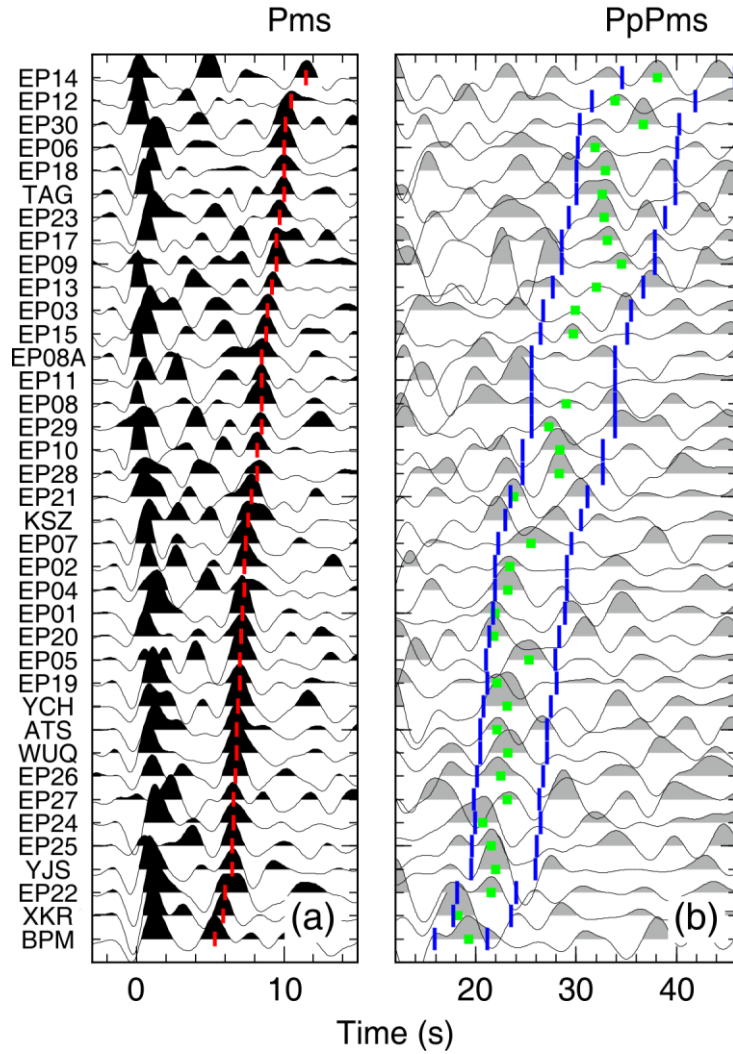
440



441

442 Figure 1. Topographic map of East Pamir showing simplified faults and locations of
 443 the seismic stations. The red triangles represent 8H stations, and the blue squares
 444 denote the CEA permanent stations. The color-coded dots mark the
 445 intermediate-depth earthquakes at depths greater than 50 km from Bloch et al. (2020).
 446 The top right inset illustrates the location of our study region (red box) relative to the
 447 India-Asia collision zone. Abbreviations are as follows: MPT, Main Pamir Thrust;
 448 PFT, Pamir Frontal Thrust; KYTS, Kashgar-Yecheng Transfer System; KKF,
 449 Karakoram fault; KXF, Karakax fault; MA, Muztagh Ata; KG, Kongur Shan; WKS,
 450 West Kunlun Shan.

451



452

453 Figure 2. Stacks of PRFs for each station with moveout corrections already completed
 454 for (a) Ps and (b) PpPs sorted by the delay time of the Moho Ps conversion. The red
 455 ticks and green squares delineate the picked arrivals of the Moho Ps and PpPs phases,
 456 respectively. The blue ticks mark the predicted time windows for the appearance of
 457 the PpPms phase at each station.

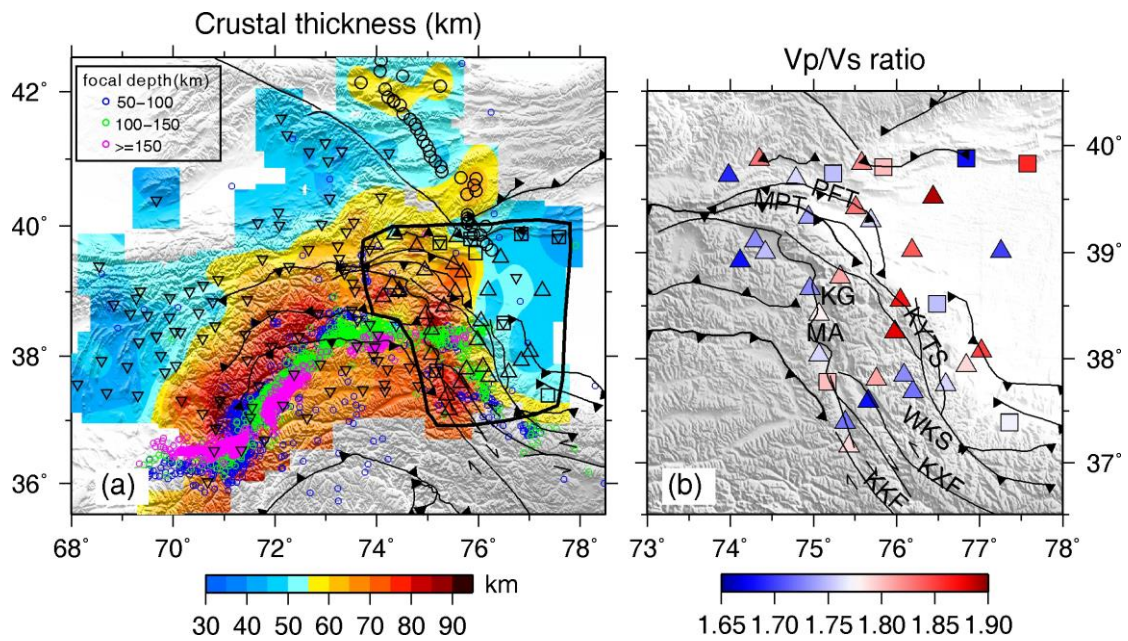
458

459

460

461

462



463

464

465 Figure 3. Maps of the (a) crustal thickness and (b) average Vp/Vs ratio. The crustal
466 thickness values from Schneider et al. (2019) and Zhang et al. (2020) have also been
467 included in Figure 3a. The intermediate-depth earthquakes at depths greater than 50
468 km from Bloch et al. (2020) are marked in Figure 3a by color-coded circles. The
469 results for the area delineated by the black line in Figure 3a are analyzed in detail in
470 this study.

471

472

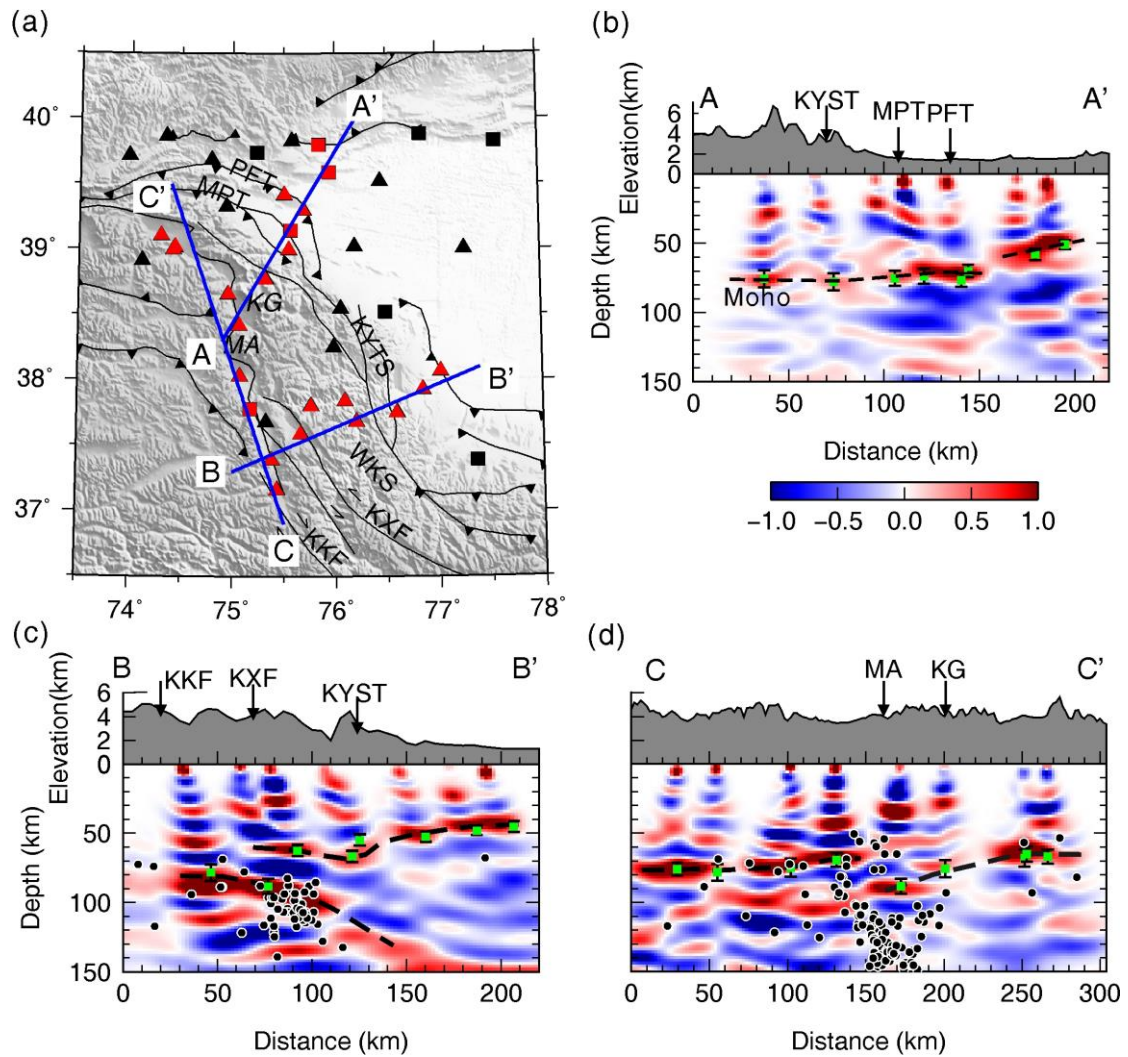
473

474

475

476

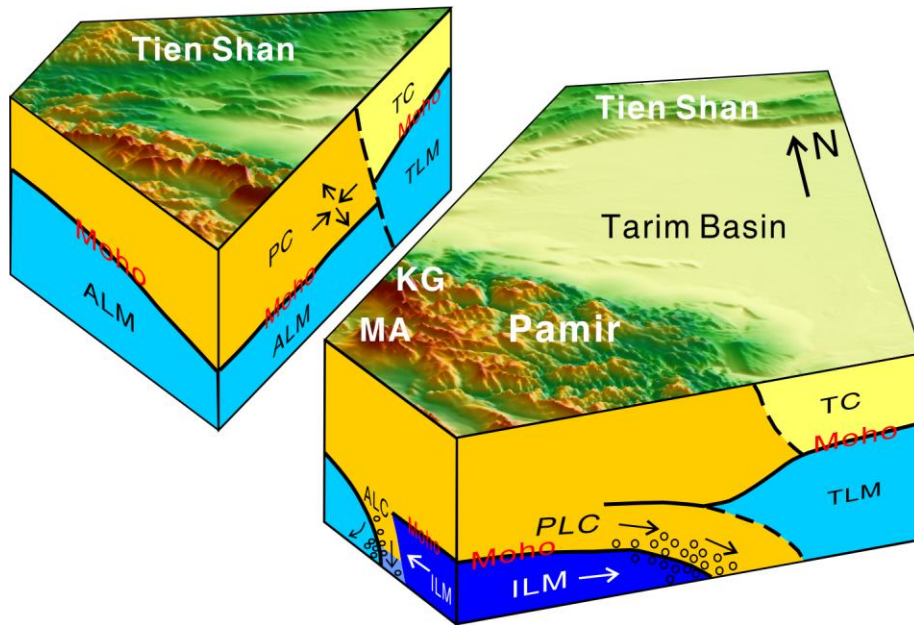
477



478

479 Figure 4. CCP stacking images along three cross sections, A-A', B-B' and C-C'. The
 480 positive (negative) amplitudes are filled in red (blue) to indicate the interfaces where
 481 the velocity increases (decreases) with depth. The resulting crustal thicknesses and
 482 errors are marked by the green squares and bars, respectively, and are superimposed
 483 on the well-resolved Moho conversions (black dashed lines). The black circles are the
 484 projected intermediate-depth earthquakes perpendicular to the profile within 50 km.
 485 The top left panel shows the locations of cross sections. Stations used in the three
 486 CCP cross sections are marked by red color.

487



489

490 Figure 5. 3-D schematic illustration for the proposed deformation patterns beneath the

491 east Pamir. The black circles are the symbolic intermediate-depth earthquakes.

492 Abbreviations are as follows: ILM, Indian lithospheric mantle; PC, Pamir crust; PLC,

493 Pamir lower crust; ALC, Asian lower crust; ALM, Asian lithospheric mantle; TC,

494 Tarim crust; TLM, Tarim lithospheric mantle.

495